THESIS FOR THE DEGREE OF DOCTOR OF PHILOSOPHY
IN THERMO AND FLUID DYNAMICS

Investigation of Tonal Noise Sources from Centrifugal Fan using Detached Eddy Simulation

MARTIN OTTERSTEN

Department of Mechanics and Maritime Sciences
Division of Fluid Dynamics

CHALMERS UNIVERSITY OF TECHNOLOGY

Gothenburg, Sweden 2022

Investigation of tonal noise sources from centrifugal fan using detached eddy simulation
MARTIN OTTERSTEN
Department of Mechanics and Maritime Science
Division of Fluid Dynamics
Chalmers University of Technology

Abstract

Since we spend the majority of our time indoors, heating, ventilation, and air conditioning (HVAC) systems have become a more and more important part of many people´s life. They provide a sufficient amount of airflow with the correct temperature, quality, and humidity. The negative side is the noise it produces and the dominant one is the tonal noise which is generated by the fan. In the fan, there is a gap between the rotating shroud and the stationary inlet duct. The pressure difference between the fan's inner and outer sides drives air to pass through the gap.

In this thesis, tonal noises at the blade passing frequency (BPF) produced by a centrifugal fan is investigated to be able to understand the generation mechanism and identify their sources. The approach is to use the hybrid method coupling the improved delayed detached eddy simulation with the acoustic analogy Formulation 1A of Farassat.

It is found that recirculating flows at the blades are associated with the gap between the shroud and the inlet duct. The turbulence that develops at the gap is swept along the shroud wall and is swept downstream to interact with the top side of the blade leading edge (BLE). The interaction renders uneven surface pressure distributions among the blades that agree with the tonal noise sources from the wall-pressure fluctuations.

Different gap geometries are studied and it is found that the gap designs affect the amplitude of the root mean square (RMS) pressure on the BLE. The spectral analysis shows that the regions with high energy correspond to the high RMS regions at the BLE and that the amplitude of the tonal noise at the BPF differs between the cases.
Also, the turbulent structures at the gap are swept downstream along the intersection between the blade and shroud, on the pressure side of the blade. They render uneven high-pressure regions in the blade passage. The high-pressure regions rotate with a speed of approximately 5% of the fan rotation speed.

Keywords: Blade passing frequency, Centrifugal fan, Computational aeroacoustics, Low-frequency rotation, Tonal noise.

Acknowledgments

List of abbreviations

Abbreviations

AHU   – Air Handling Unite

BPF   – Blade Passing Frequency

BLE   – Blade Leading Edge

BTE   – Blade Trailing edge

CFD   – Computational Fluid Dynamics

CAA   – Computational Aeroacoustics

IEQ   – Indoor Environmental Quality

HVAC   – Heating, Ventilating, and Air Conditioning

PSD   – Power Spectral Density

RMS   – Root Mean Square

SPL   – Sound Pressure Level

TKE   – Modeled Turbulence Kinetic Energy

Thesis

This thesis consists of an extended summary and the following appended papers:

Paper I   M. Ottersten, H.-D. Yao, and L. Davidson, "Unsteady Simulation of tonal noise from isolated centrifugal fan," Conference paper FAN2018. Darmstadt, Germany, (2018)

Paper II   M. Ottersten, H.-D. Yao, and L. Davidson, "Tonal noise of voluteless centrifugal fan generated by turbulence stemming from upstream inlet gap," Phys. Fluids, 33, (2021). https://doi.org/10.1063/5.0055242. (Editor´s pick).

Paper III   M. Ottersten, H.-D. Yao, and L. Davidson, "Inlet gap effect on tonal noise generated from a voluteless centrifugal fan," Conference paper FAN2022. Senlis, France, (2022). Selected by the committee for publication in the International Journal of Turbomachinery, Propulsion and Power.

Paper IV   M. Ottersten, H.-D. Yao, and L. Davidson, "Inlet gap effect on aerodynamics and tonal noise generated from a voluteless centrifugal fan," positive first review, Journal of Sound and Vibrations, (2022)

Paper V   M. Ottersten, H.-D. Yao, and L. Davidson, "Inlet gap influence on low-frequency rotation in a centrifugal fan at high mass flow," To be submitted to a scientific journal, (2022)

Paper VI   M. Ottersten, H.-D. Yao, and L. Davidson, "Effect of micro vortex generators on tonal noise from a centrifugal fan," Conference paper ICA2022, October 24 – 28, Gyeongju, Korea, (2022),

Other publications

Paper VII   M. Ottersten, H.-D. Yao, and L. Davidson, "Numerical and experimental study of tonal noise sources at the outlet of an isolated centrifugal fan," (2020) arXiv:2011.13645.

Patent A   M. Ottersten, Inventors; Swegon AB, applicant. "Fan for Air Handling Unit – Increasing efficiency," *Submitted*, (2019)

Patent B   M. Ottersten, Inventors; Swegon AB, applicant. "Fan for Air Handling Unit – Increase strength," International patent WO 2021034260, (2021)

Patent C   M. Ottersten, Inventors; Swegon AB, applicant. "Accessory to Fan for Air Handling Unit – Increase efficiency and decreases noise," International patent WO *2021194409*, (2021)

Patent D   M. Ottersten, Inventors; Swegon AB, applicant. "Fan for Air Handling Unit – Decrease Tonal Noise at BPF," *Submitted*, (2022)

Division of work

Besides being the main author for all papers. My contribution consisted of; developing and designing the centrifugal fans, performing all the CFD simulations, post-processing, and analyzing the results. Prof. L. Davidson has been the main supervisor and Associate Prof. H.-D. Yao the co-supervisor. They provided guidance and helpful discussions, and assisted in the interpretations of the results.

x

Content

1. Introduction

1.1 Background

Today most people spend the majority of their time indoors, up to 90 % [1]. The indoor environmental quality (IEQ) has become more and more important. When considering IEQ we usually think about temperature, CO_2 level, and humidity. However, it has been established that sound quality is also an important factor for high-quality IEQ [2, 3]. Noise is harmful to human's health not only by directly causing loss of hearing and tinnitus but also by indirectly producing annoyance, sleep disturbance, and stress [4]. All of these will affect performance and well-being. It was reported in [5] that noise has a detrimental effect on reading and writing and that the cognitive development in children is affected by chronic exposure to noise.

1.2 The HVAC system

The structure of modern buildings is good at reducing external noise from traffic, and significant improvements have been made over recent years [6]. Although the internal noise from heating, ventilation, and air conditioning (HVAC) systems is difficult to isolate. One of the functions of HVAC systems is to control the temperature, the quality, and the humidity in the airflow. An air handling unit (AHU) is designated for the controlling. It moves and cleans air, as well as recovers latent and sensible heat in the air. As illustrated in Figure 1, a modern AHU usually consists of a fan, a filter, and two channels such as a supply and an extract. AHU is known as dominant noise contributors
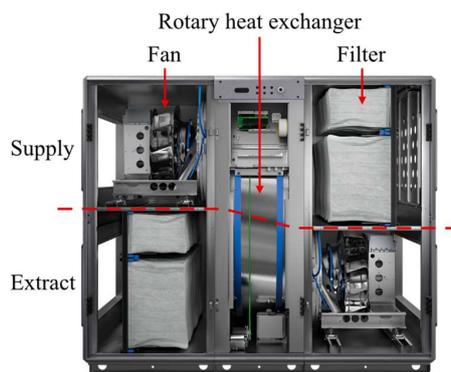

Figure 1. Swegon´s AHU - Gold 12 RX.

1.3 Centrifugal fan

The tonal noise in an AHU is mainly produced by the fan component. Therefore, the present study is organized to specifically investigate an isolated fan, i.e. without the AHU. The fan is of the centrifugal type running at low speeds, to satisfy the requirements of small size and high pressure airflow [7]. In the AHU the centrifugal fan is usually without the stationary volutes, to improve the aerodynamic and aeroacoustic performances. Volutes for radial-flow turbomachines (e.g., centrifugal fans and pumps) are spiral funnel-shaped casings that house rotors. Their function is to guide the flow from rotors to outlets and maintain constant flow speeds. The treatment of removing volutes is termed voluteless hereafter.

Regarding the structure of the fan part, a shroud and a backplate are assembled onto the top and bottom sides of the rotating blades, respectively, visualized in Figure 2b. The numerical setup for the fan is illustrated in Figure 2. There are two ducts, which are placed upstream and downstream of the fan. The flow at the inlet is undisturbed with a uniform velocity profile. There is a gap (colored blue) between the rotating fan shroud and the stationary inlet duct, this to separate the rotating part from the stationary part. The pressure difference between the fan's inner and outer sides drives air to pass through the gap. As displayed in Figure 2a, the fan and inlet duct are placed in a downstream duct, and the inlet duct is connected to an upstream duct. There are two microphones, M1 upstream of the fan and M2 downstream of the fan. This simple geometry layout is designed for the numerical simulations. This simplification reduces the geometry complexity but retains the principal flow and acoustic characteristics. The fan parameters are listed in Table 1.
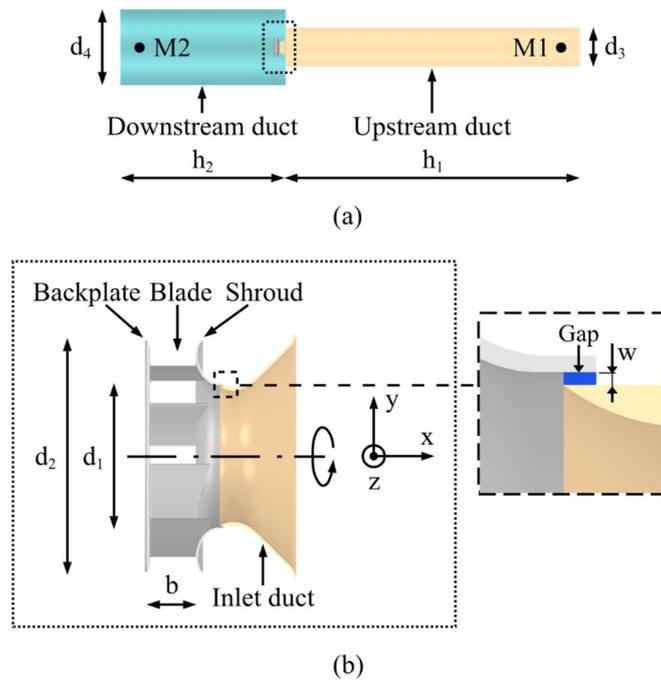
Figure 2. a) The simple geometry layout for the numerical simulations. Here M1 and M2 mark out two microphone positions. b) The fan configuration and inlet duct. The gap is colored blue. The rotation axis of the fan is the x-axis.

Table 1. The fan parameters.

d_1	d_2	d_3	d_4	b	h_1	h_2	w
0.165 m	0.268 m	0.6 m	1.1 m	0.053 m	4.0 m	2.3 m	1.5 mm

1.4 Fan generated noise

The rotating fan produces turbulent flows which generate noise, with both broadband and tonal parts [8]. The fan tonal noise generation is attributed to multiple causes. Pressure and density fluctuations on fan blades are identified as dominant sources in a large body of studies, e.g., by Ffowcs Williams and Hawkings [9]. A typical mechanism of tonal noise at the blade passing frequency (BPF) is the interaction between a helical unsteady inlet vortex and the rotating blades near the fan backplate [10]. In addition, another type of potential tonal noise source is coherent flow structures like those in vortex shedding.

Tonal noise at the BPF is a well-known problem for HVAC system manufactories. The noise can be reduced by placing silencers in ducts, but the silencers introduce additional pressure loss. Besides, the silencers are mainly effective in absorbing broadband noise rather

3

than tonal noise. They can be tuned to dampen the tonal noise at specific frequencies, while the tuning is not valid for a wide range of frequencies [11]. The frequency of the tonal noise at the BPF is connected to the rotation speed of the fan. In variable air volume (VAV) systems the fan speed changes continuously to meet the demand. It means that the tonal noise changes continuously over a wide range of frequencies, which decreases the effect of the silencers.

Today noise requirements in buildings are measured in 1/3 octave bands. Due to this, the noise characteristics of HVAC systems are unknown. The sound pressure level (SPL) measured in an experimental rig for one of Swegon´s centrifugal fans is shown in Figure 3. For the 1/3 octave band, the tonal noise at the BPF is masked and the correct noise characteristics are not shown. When the HVAC system is installed this can cause noise problems in the building.
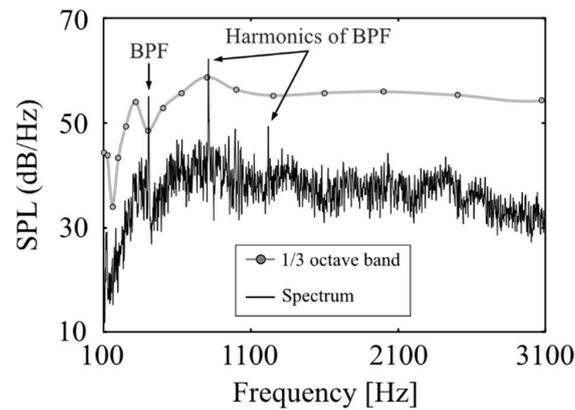

Figure 3. SPL of the sound downstream of the fan.

1.5   Operation point

The fan rotation speed is 2800 rpm (revolutions per minute). Given that the fan has 7 blades, the blade passing frequency BPF is 326.7 Hz, and the first harmonic frequency is 653.4 Hz. The Mach number based on the tip velocity is 0.1.

The fan characteristic curve is shown in Figure 4a. Five operation points are measured. The maximum efficiency point is found between Points 2 and 3, where the pressure rise is 410.83 Pa and the mass flow rate is 0.36 kg/s. The power spectral density (PSD) of the tonal noise at the BPF is shown in Figure 4b. The noise increases at the off-design condition Point 4, where the pressure rise is 269.65 Pa and the mass flow rate is 0.467 kg/s. Hence, Point 4 is specifically studied to understand the causes of the noise increase.
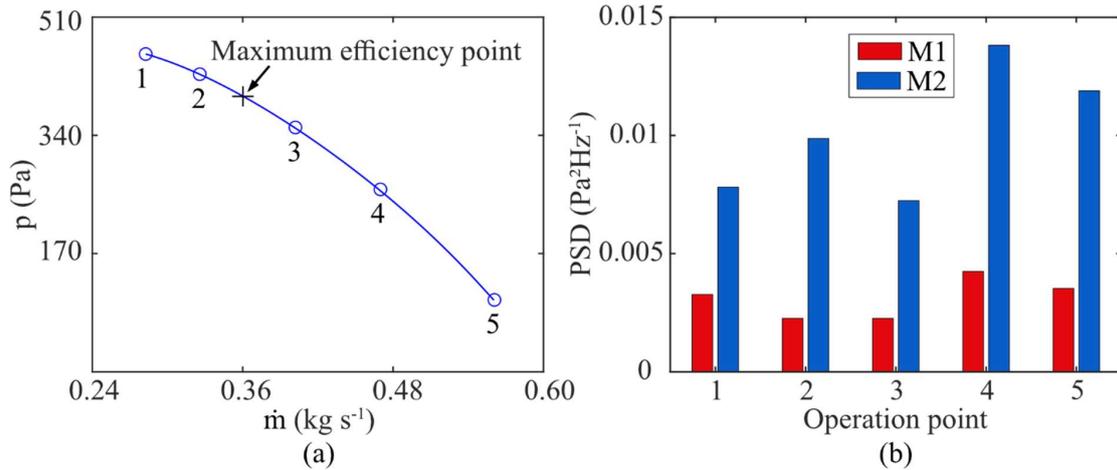
4

Figure 4. a) The fan characteristic curve at the fan rotation speed of 2800 rpm. The operation points labeled with circles are further measured for the tonal noise. b) The PSD of the tonal noise at the blade passing frequency *BPF* for the upstream microphone (M1) and the downstream microphone (M2).

1.6   Motivation of the thesis

Three different cases were tested at Swegon to investigate the helical unsteady inlet vortex that interacts with the rotating blades near the fan backplate [10]. The cases are illustrated in Figure 5. A flow straightening structure (also termed honeycomb (HC) colored brown) was assembled before the inlet duct, to straighten the inlet flow. A vortex-affecter (colored green) was placed inside the fan in Cases B and C to affect the helical unsteady inlet vortex. For Case C it was flipped and moved away from the backplate so that the largest diameter is at the location of the gap. The three cases are described in Table 2. The sound pressure level for the three cases is shown in Figure 6. The amplitude of the tonal noise at the BPF is decreased for Case C, compared to Case A and for Case B it is almost the same. The author realized that there have to be something else than the helical unsteady inlet vortex that interact with the blades. These results motivated the author to do this thesis.
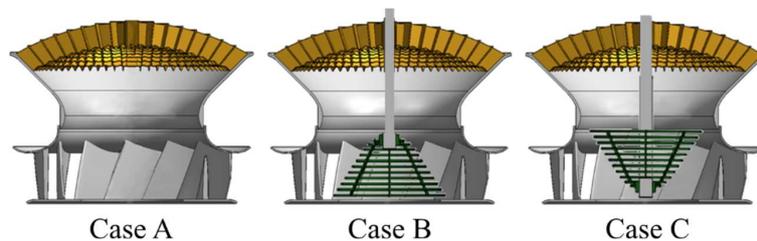

Figure 5. Geometry setup, honeycomb colored brown and vortex-affecter colored green.

Table 2. Description of the cases

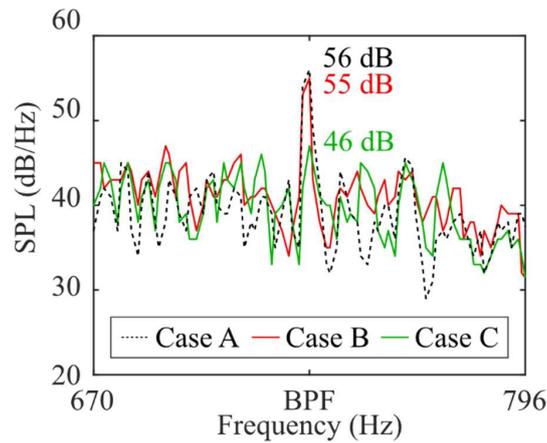|	HC before the inlet duct	Vortex-affecter
Case A (reference)	Yes	-
Case B	Yes	Yes
Case C	Yes	Yes, flipped and moved

Figure 6. Sound pressure level for Case A, B, and C at the BPF.

1.7   Aim

This study is aimed at developing a hybrid computational aeroacoustics (CAA) method to accurately predict the fan tonal noise, in particular, at BPF. The mechanisms of the tonal noise generation will be explored and the noise sources will be identified. Moreover, different fan geometries will be studied to investigate if the amplitude of the BPF can be decreased. The hybrid CAA method couples a computational fluid dynamics (CFD) method with the Ffowcs Williams and Hawkings (FW-H) acoustic analogy. The CFD method is the improved delayed detached eddy simulation (IDDES). Formulation 1A of the FW-H acoustic analogy is chosen. The CAA method will be validated based on experiments.

2. Methods

Understanding and predicting tonal noise is not easy since the noise has much lower energy than the flow. A convenient method is to use an acoustic analogy. The acoustic analogy was first proposed by Lighthill [12]. The basic principle of the acoustic analogy is to separate the computation of the noise generation and propagation from the flow simulation. The theory has been developed into a family of methods, in which the FW-H analogy is the most popular one. In this study, a hybrid approach coupling various CFD methods with the FW-H analogy is employed. The unsteady flow field is simulated using the unsteady RANS [13] and the Improved Delayed Detached Eddy Simulation (IDDES) [14]. The FW-H analogy is implemented with Formulation 1A [15].

The air is considered an ideal gas. The flow is compressible. A finite volume method is utilized to discretize the continuity, momentum, and energy equations. The method employs a segregated flow solver accomplished with the Semi-Implicit Method for Pressure-Linked Equations (SIMPLE) algorithm [16].

The convection flux on a cell face is discretized utilizing a hybrid second-order upwind and bounded scheme. The diffusion fluxes on both internal and boundary cell faces are discretized with a second-order scheme. The second-order hybrid Gauss-LSQ method is used in gradient computation. A second-order implicit method is taken to discretize the time derivative. The time marching procedure adopts inner iterations at every preconditioned pseudo-time step. The simulations in Paper II-VI are performed using the commercial software STAR-CCM+ [17]. This setup was validated in the previous study [18], where turbulence-induced acoustic waves transmitting through a cabin window were simulated. The ANSYS FLUENT is used in Paper I, see section 2.2. Swegon uses the software FLUENT and the simulations for Paper I, was executed at Swegon.

2.1 Governing equations

The transport equations of continuity, momentum, and energy equations in the conservation form, which are solved by CFD solvers, are generally written as

$$\frac{\partial \rho}{\partial t} + \nabla \cdot (\rho \boldsymbol{u}) = 0,$$

$$\frac{\partial (\rho \boldsymbol{u})}{\partial t} + \nabla \cdot (\rho \boldsymbol{u} \otimes \boldsymbol{u}) = -\nabla p + \nabla \cdot \boldsymbol{\tau},$$

$$\frac{\partial}{\partial t}(\rho E) + \nabla \cdot (\rho E \boldsymbol{u}) = \nabla \cdot (k \nabla T) - \nabla \cdot (\rho \cdot \boldsymbol{u}) + \nabla \cdot (\boldsymbol{u} \cdot \boldsymbol{\tau}) \tag{1}$$

7

where the total energy $E = e + \mathbf{u} \cdot \mathbf{u}/2$, and e is the internal energy.

If the compressibility is taken into account, the viscous stress tensor $\boldsymbol{\tau}$ is defined as

$$\boldsymbol{\tau} = \mu[\nabla u + (\nabla u)^T] - \frac{2}{3}\mu(\nabla \cdot u)I \tag{2}$$

where μ is the dynamic viscosity.

2.2 URANS

The URANS method is used in the first part of this study (Paper I). The flow is incompressible. The turbulence is modeled using the k-ω shear-stress transport (SST) model. The segregated flow solver is used to solve the discretized equations. The pressure-velocity coupling approach is adopted for the SIMPLEC (Semi-Implicit Method for Pressure-Linked Equations-Consistent) algorithm. A bounded second-order implicit method is used to discretize the time derivative. The simulations are performed using the software ANSYS Fluent [13].

2.3 IDDES

The turbulence is simulated using the IDDES [14] method in this study, the simulations are performed using the software STAR-CCM+ [17]. The IDDES is combined with the k-ω SST turbulence model. This setup has been tested in several studies on rotating machinery [19, 20]. The IDDES modifies the dissipation in the transport equation of the turbulence kinetic energy k by introducing a hybrid length scale

$$\tilde{l}_{DDES} = \tilde{f}_d(1 + f_e)l_{RANS} + (1 - \tilde{f}_d)l_{LES} \tag{3}$$

where l_{RANS} and l_{LES} are the Reynolds-averaged Navier-Stokes equations (RANS) and LES length scales, respectively. The $\tilde{f}_d$ function blends between RANS and LES and the $\tilde{f}_e$ function slightly enhances the RANS content in the RANS region. And they are formulated as

$$\tilde{f}_d = \max\{\tanh(C_{dt}r_{dt})^3, \min[2\exp(-9\alpha^2), 1]\},$$
$$\alpha = 0.25 - d_w/h_{max} \tag{4}$$

where d_w denotes the distance to the wall, and h_{max} is the maximum local grid spacing. The parameter r_{dt} is defined as

$$r_{dt} = \mu_\tau/(\rho\sqrt{\nabla\mathbf{u}:\nabla\mathbf{u}^T}\kappa^2 d_w^2) \tag{5}$$

where μ_τ is the turbulent eddy viscosity, and the von Karman constant $\kappa = 0.41$. The formulation of f_e reads

$$f_e = max[(f_{e1} - 1), 0]\psi f_{e2} \tag{6}$$

where ψ is a low-Reynolds correction that rectifies the activated low-Reynolds number terms of the background RANS model in LES mode [21] The parameters in Eq. 6 reads

$$f_{e1} = \begin{cases} 2\exp(-11.09\alpha^2), & \text{for } \alpha \geq 0 \\ 2\exp(-9\alpha^2), & \text{for } \alpha < 0, \end{cases}$$

$$f_{e2} = 1 - max[\tanh(C_t^2 r_{dt})^3, \tanh(C_l^2 r_{dl})^{10}],$$

$$r_{dl} = \mu/(\rho\sqrt{\nabla\boldsymbol{u}:\nabla\boldsymbol{u}^T}\kappa^2 d_w^2) \tag{7}$$

The coefficients of the IDDES model adopts the default values in the software STAR-CCM+,i.e. $C_{DES,k-\omega} = 0.78, C_{DES,k-\varepsilon} = 0.61, C_{dt} = 20, C_l = 5$, and $C_t = 1.87$ [17]. The notation of the coefficients is the same as in the software user guide [17]. The wall-normal sizes of the first layer cells near all walls fulfill $\Delta y^+ < 1$.

2.4 FW-H equation

A hybrid approach is adopted to predict the noise generated from the flow. In this approach, the IDDES is coupled with Formulation 1A of Farassat [21]. The ambient air density is set to $\rho_0 = 1.225$ kg/m^3, and the speed of sound $c_0 = 340$ m/s. The Formulation 1A reads

$$p'(\boldsymbol{x}, t) = \frac{1}{4\pi} \int_{f=0} \left\{ \frac{1}{1 - M_r} \frac{\partial}{\partial \tau} \left[\frac{\rho_0 v_n}{r(1 - M_r)} + \frac{p \cos\theta}{c_0 r(1 - M_r)} \right] \right\}_{\tau_e} dS$$

$$+ \frac{1}{4\pi} \int_{f=0} \left[\frac{p \cos\theta}{r^2(1 - M_r)} \right]_{\tau_e} dS \tag{8}$$

where $r = |\boldsymbol{x} - \boldsymbol{y}|$, and $M_r = (\boldsymbol{x} - \boldsymbol{y}) \cdot \boldsymbol{v}/(rc_0)$. The variable v_n is the local surface normal velocity, and τ_e denotes the emission time. Besides, $\cos\theta = (\boldsymbol{x} - \boldsymbol{y}) \cdot \boldsymbol{n}$, where $\boldsymbol{n}$ is the unit vector normal to the surface.

According to Neise [22], the fan noise generation at low Mach numbers is dominated by dipole noise sources that are derived based on the FW-H equation. Hence, the noise prediction in this study considers only an impermeable integral surface for Formulation 1A which means that $v_n = 0$. The integral surface consists of the fan blades, shroud, and backplate (see Figure 1a), this approach is chosen so that the sources for the BPF can be identified. This method agreed well in [23] where the unsteady flow in a centrifugal fan was studied and evaluated with experiments. The upstream and downstream ducts, as well as the fan inlet duct, are neglected. This treatment disregards the acoustic reflection from the duct walls to resemble the conditions in the experimental rig.

2.5 Numerical settings

The entire computational domain is divided into stationary and rotating parts. The parts contained within the ducts are stationary, whereas the part inside the fan is rotary. The rotating part is set to rigid body motion. The meshes of the stationary and rotary meshes are not conformable at the interfaces between them.

The under-relaxation factors for the velocity and pressure in the segregated flow solver are set to 0.7 and 0.4, respectively. The under-relaxation factor for the turbulence equations is 0.7. The mass-flow boundary condition is set at the inlet, with a uniform velocity distribution. The modeled turbulence intensity is set to $I = 4\%$ according to $I = 0.16(R_e)^{-1/8}$ [29]. Here R_e is computed based on the inlet diameter and the streamwise velocity at the inlet. The modeled turbulence length scale is set to $\ell = 0.05$ m based on $\ell = 0.7d_3$ where d_3 is the upstream duct diameter. The pressure-outlet boundary condition is set at the outlet with the static pressure of 101325 Pa, which is the reference pressure (p_{ref}) in the ambient air. The no-slip boundary condition is specified on all walls.

2.6 Local mesh refinement

In Paper II, a local mesh refinement study was performed inside the fan at the regions extending from the gap to the blade leading edge (BLE) and along the blade to the blade trailing edge (BTE). Here high TKE was found due to gap turbulence in Paper I. These mesh refinement regions (blue) are illustrated in Figure 7. The mesh parameters are listed in Table 3. The refined mesh resolution enables the LES mode for the IDDES, which is controlled by $\tilde{f}_d$ in Eq. 4. $\tilde{f}_d$ blends between the URANS and LES mode, which depends on the grid spacing and the wall distance.

   The mesh size in the upstream duct and downstream duct is 55 cells per meter. According to [17] it should be at least 20 cells per wavelength for the shortest wavelength. This corresponds to a minimum frequency of 124 Hz for this mesh, which is well below the tonal noise at the BPF = 326.7 Hz.
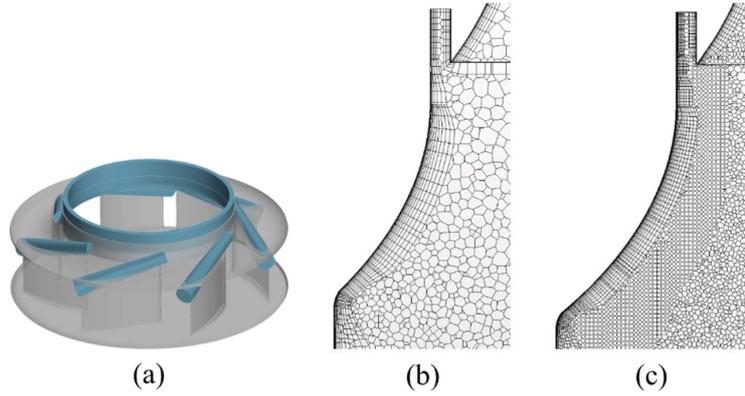
Figure. 7. a) Mesh refinement regions (blue) at the inlet gap and blades top region. Mesh cells near the inlet gap in b) the Coarse-mesh and c) the Refined-mesh.

Table 3. The mesh parameters.

	Coarse-mesh	Refined-mesh	Less-refined†	Ultra-refined†
Refinement factor	-	1	0.85	1.15
Total number of cells	32×10^6	52×10^6	46.5×10^6	58.3×10^6
Number of cells in rotating zone	22.9×10^6	41.9×10^6	36.4×10^6	48.2×10^6
Maximum Δy^+ near blade walls	0.93	0.73	0.83	0.65
Cell growth ratio	1.05	1.05	1.05	1.05

† The less-/ultra-refined meshes are generated by adjusting the cell sizes of the refined mesh in the rotating zone.

Important physical quantities describing the fan performance are the static pressure rise, which is between the fan inlet and outlet, and the fan torque. These two quantities from the four meshes are listed in Table 4. The results of Refined-mesh and Ultra-refined agree well with the experimental data.

The comparison of Refined-mesh, Less-refined, and Ultra-refined shows that the mesh refinement in the rotating zone leads to converged results.

Table 4. Fan performance data.

	Static pressure rise (Pa)	Torque (N·m)
Coarse mesh	255.61	1.133
Less-refined	262.12	1.129
Refined-mesh	267.82	1.127
Ultra-refined	267.91	1.127
Experiment	269.65	1.125

The contours of vorticity magnitudes $\|\vec{\omega}\|$ near the fan inlet gap are shown in Figure 8. In contrast to the Coarse-mesh, the Refined-mesh resolves turbulent vortices that originate from the gap. The reason is that the fine mesh resolution turns on the LES mode of the IDDES [24].

The gap turbulence is mixed with the main flow as it is swept downstream. For the sake of brevity, Refined-mesh is chosen for the analysis and discussion hereafter.
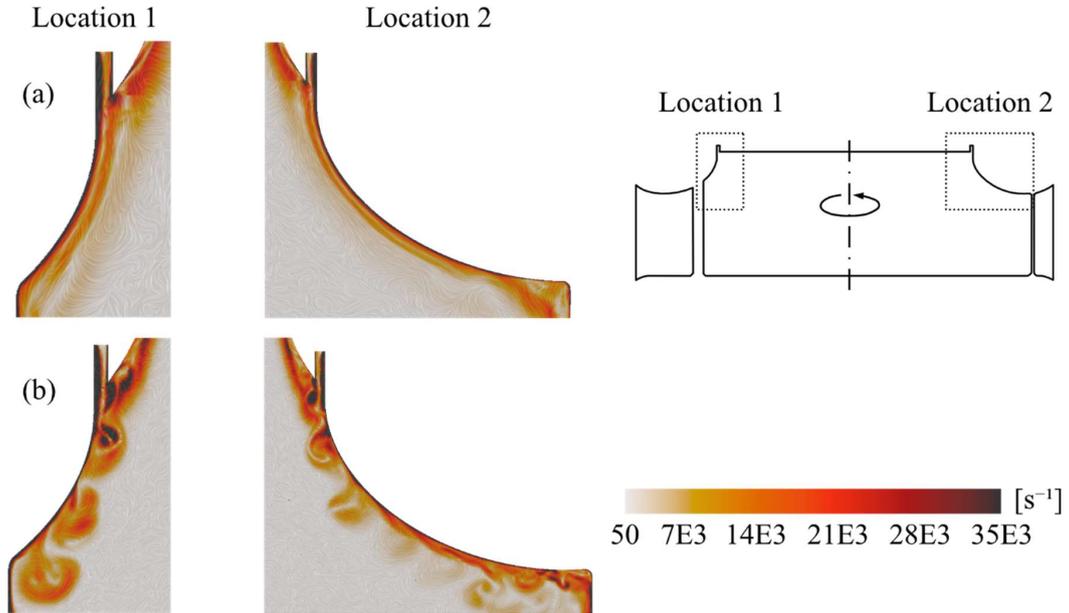

Figure. 8. Instantaneous vorticity magnitudes near the inlet gap. a) Coarse-mesh; b) Refined-mesh.

3. Results

3.1 Direct noise computation (DNC)

Four monitor points, PI, PII, PIII, and PIV, are set to observe the pressure, as shown in Figure 9a. PI and PII are located in the downstream duct, and PIII and PIV are located in the upstream duct. The time history of the pressure at the monitoring point, PI, excluding the reference pressure ($p_{ref} = 101325$ Pa), is displayed in Figure 9b. The Power Spectral Density (PSD) of the pressure in these points, could not show the tonal frequency at the BPF. The root mean square (RMS) of the pressure in PI is, $RMS_{DNC\_PI} = 0.71$ Pa and the RMS of the FW-H sound pressure in M1 is, $RMS_{FW-H\_M1} = 0.36$ Pa. The pressure fluctuations are higher in the airflow at this point than the sound pressure fluctuations. This method was therefore abandoned and we only used the hybrid approach coupling various CFD methods with the FW-H analogy in this study. The hybrid approach is also chosen so that the sources for the BPF can be identified.

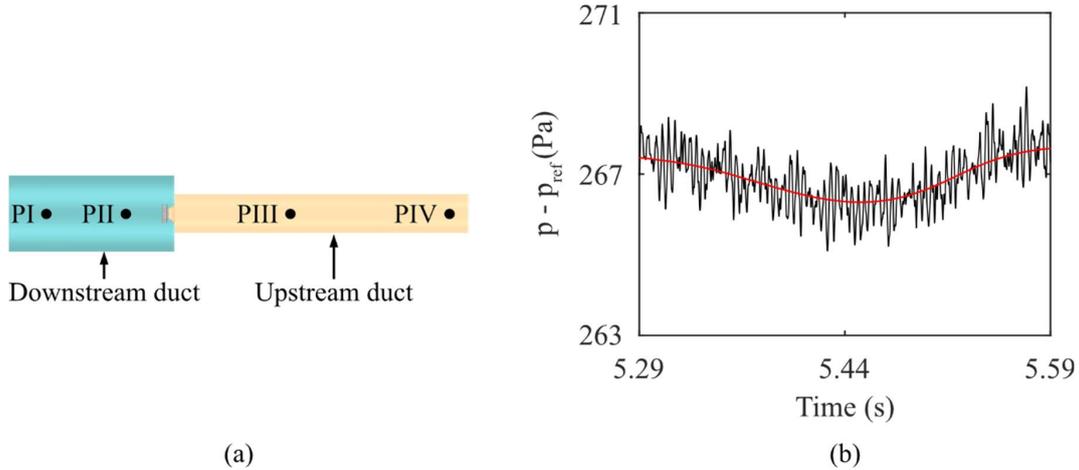|	
(a)	(b)

Figure 9. a) Monitor points PI, PII, PIII, and PIV. b) The time history of the pressure at PI. The red line is a Gaussian function fitted to the instantaneous pressure.

3.2 Gap flow (Paper I)

The fan performance is influenced by the flow separation on the blades. The separation is identified based on the wall shear stress. Figure 10 shows that there is recirculating flow at the blade near the shroud. Low wall shear stress is observed near the BTE. Furthermore, it is found that the recirculating flow originates from the fan gap, as illustrated in Figure 11.
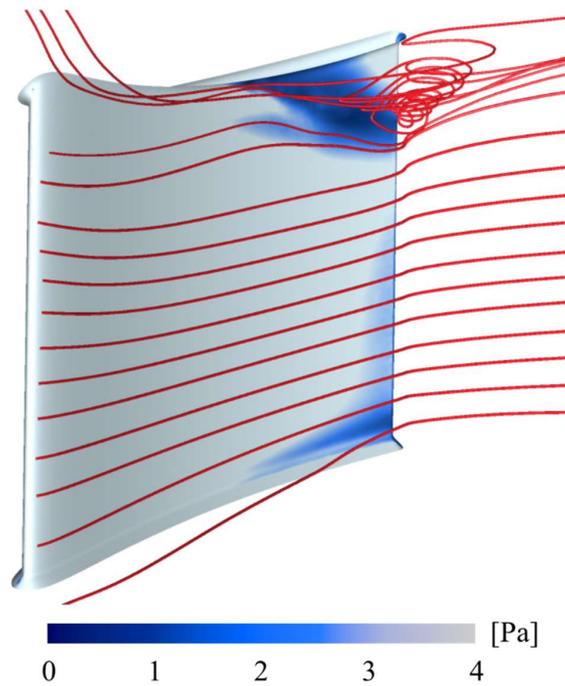
13

Figure 10. Contour plot of the wall shear stress at the blade with airflow visualized with streamlines
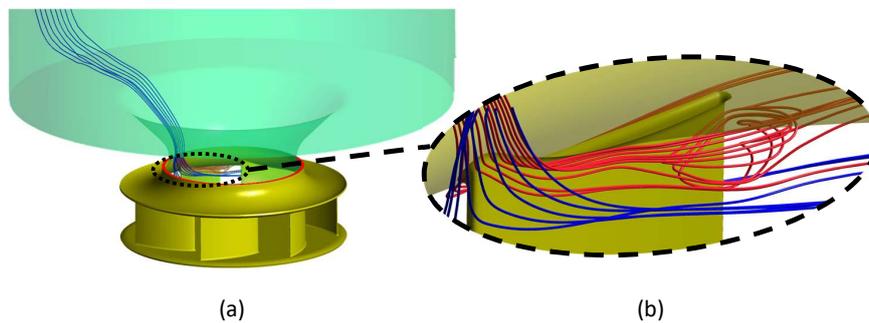

(a)　　　　　　　　　　　　　　　(b)

Figure 11. Streamlines starting from the inlet (blue) and the gap (red). The gap is shown in Figure 1. a) The fan and inlet duct, b) A magnified view of the blade and shroud intersection.

The Power Spectral Density (PSD) of the noise at the microphones, M1 and M2 are shown in Figure 12. The tones measured at M1 agree well with the experimental result. At M2, the tones do not agree well. The noise characteristic may be affected by the flow through the fan and the material in the fan and surrounding structures [25, 26].
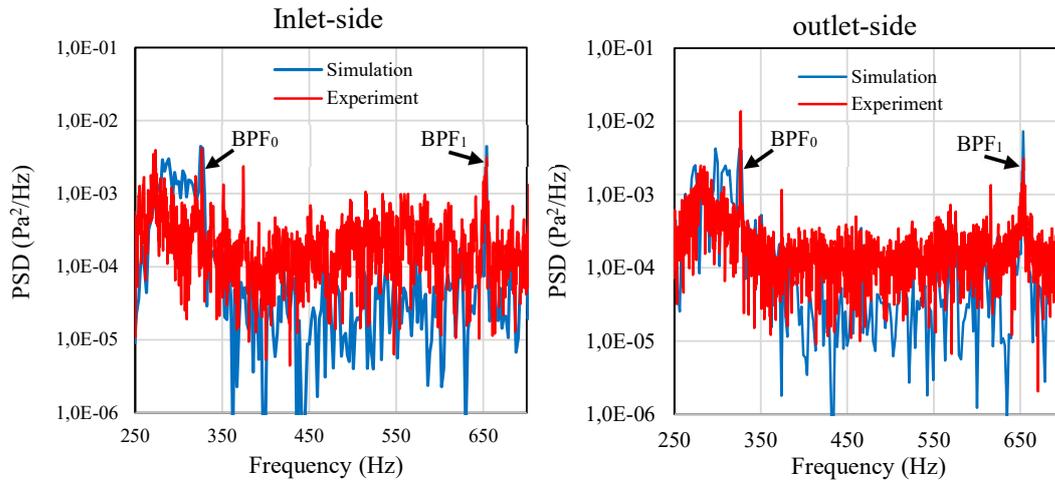
Figure 12. Comparison of PSD at the inlet-side (M1) and outlet-side (M2).

3.3 Turbulence from inlet gap (Paper II and Paper III)

Compared with the mesh used in Paper I, the mesh is refined in all regions and especially in the gap and the blade regions. Turbulence develops in the gap between the rotating fan and the stationary inlet duct, as indicated by visualizing vorticity magnitudes near the gap in Figure 13.
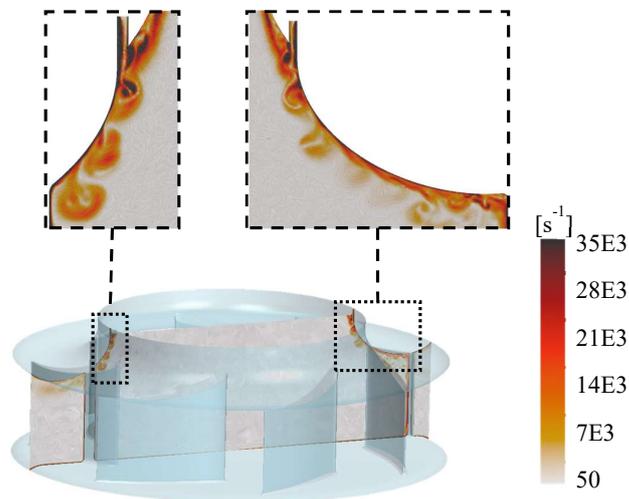

Figure 13. Instantaneous vorticity magnitude near the inlet gap.

The contours of vorticity magnitudes $\|\vec{\omega}\|$ at the blade leading edge for Case 1 are shown in Figure 14a. There are regions with high vorticity magnitude close to the shroud. They are generated when the gap flow is mixed with the main flow. This phenomenon was also

15

observed in previous studies [27]. The black dashed line is a monitoring line positioned at the BLE which extends from the backplate to the shroud. The line follows the blade rotation and the surface pressure is monitored at one blade during 12 fan revolutions. The RMS of the surface pressure is shown in Figure 14b. At the position nearest the shroud, the RMS has its highest value. As the distance to the shroud increases, the RMS pressure decays. At the backplate, the RMS pressure is 5 Pa, which is approximately 4% of the value at the shroud (128 Pa).
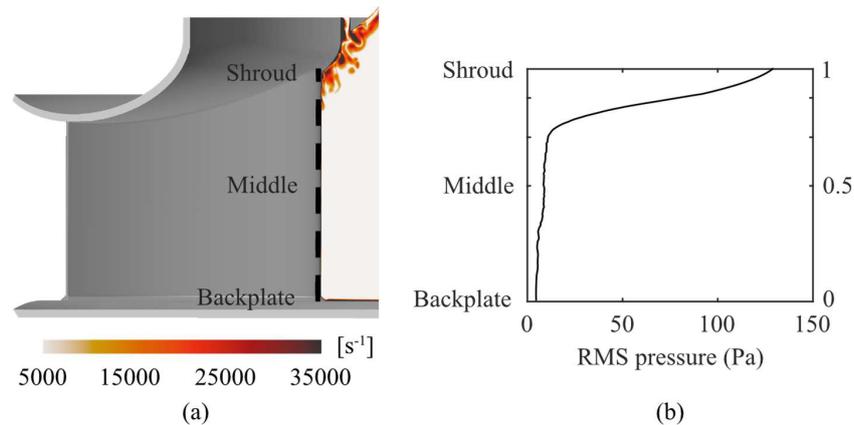

Figure 14. a) Vorticity magnitude $\|\vec{\omega}\|$ at one blade. The black dashed line marks the monitoring line at the BLE; b) the RMS of the pressure fluctuations with respect to the normalized length along the monitoring line

The time history of the surface pressure at the monitoring line is shown in Figure 15. At the position shroud, the pressure fluctuates with large amplitudes and high frequencies. As the distance from the shroud increases the amplitudes of pressure fluctuations decrease. Small fluctuations are observed at the middle position. At the backplate, fluctuations are almost negligible.

Moreover, a periodic low-frequency fluctuation in relation to the fan revolution is observed. By comparing the three monitoring points, high-frequency fluctuations decay rapidly with increased distance to the shroud. The periodic low frequency is predominant at the middle position and at the backplate.
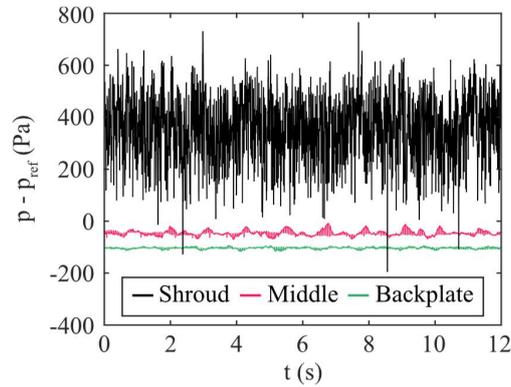
Figure 15. The time history of surface pressure fluctuations at three locations along the BLE

Based on the band filtered PSD of the wall pressure fluctuations, it is possible to find the noise sources. The surface pressure levels (SPL) at the tonal frequencies, 273 Hz, 326.7 Hz (BPF), and 653.3 Hz (the first harmonic of BPF) are illustrated in Figure 16. The highest PSD at all tonal frequencies are located at the blade leading edge close to the shroud.
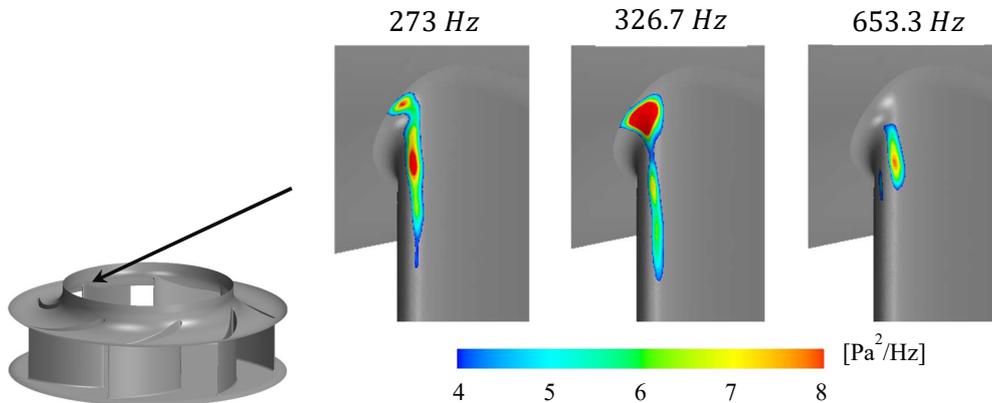

Figure. 16. SPL of the surface pressure fluctuations at three tonal frequencies.

3.4 Inlet gap effect on fan performance (Paper III and Paper IV)

Different gap geometries and designs are studied in Paper III (Cases 1, 2, and 3) and in Paper IV (Cases 1, 2, 3, and 4). The baseline fan (Case 1) and the three different designs (Case 2, Case 3, and Case 4) are illustrated in Figure 17. Case 1 is the same fan as the one examined in Paper I, II, V, and VI. The fan backplate and blades are the same for all cases and there are seven blades. For Cases 1, 2, and 3 the shroud geometry is the same, and the flow path of the gap is straight in the x-direction. Case 2 has a larger gap width (denoted by w), and Case 3 has

17

a smaller one than Case 1. The gap width is varied by changing the wall thickness of the inlet duct. In comparison to the other cases, a curved flow path of the gap is designed for Case 4, while its gap width is the same as Case 1. The gap width is given in Table 5.
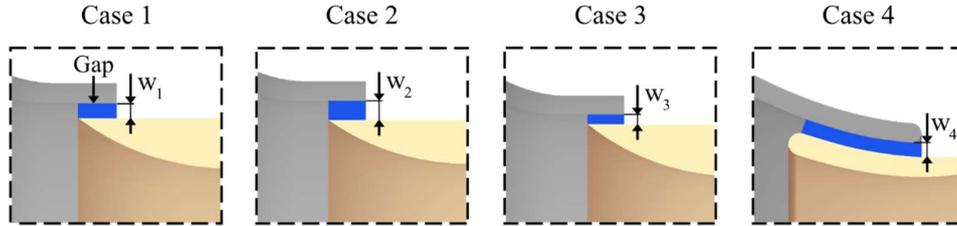

Figure 17. Case 1 (baseline), Case 2 (larger gap width), Case 3 (smaller gap width), and Case 4 (curved gap, same gap width)

Table 5. The gap width.

w_1	w_2	w_3	w_4
1.5 mm	2.0 mm	1.0 mm	1.5 mm

The fan performance is compared for the different gap design cases described in Figure 17. The static pressure excluding the reference pressure ($p_{ref} = 101325$ Pa) is displayed along the axial symmetric line for all cases in Figure 18. All cases show consistent pressure amplitudes in the upstream duct of the fan, while differences are seen downstream. The difference in pressure rise downstream of the fan is only due to the gap design. Compared to Case 1, the gap width is larger in Case 2 and smaller in Case 3. Among these three cases, the pressure rise is smallest in Case 2 and largest in Case 3. Therefore, increasing the gap width worsens the fan performance. However, the anomaly is found in Case 4. This case produces larger pressure rise than Cases 1-3, even though its gap width is the same as Case 1. The geometric differences between Cases 1 and 4 are that the gap wall of Case 4 has a longer streamwise length and a curved shape. These geometric changes lead to an increase in the pressure rise.
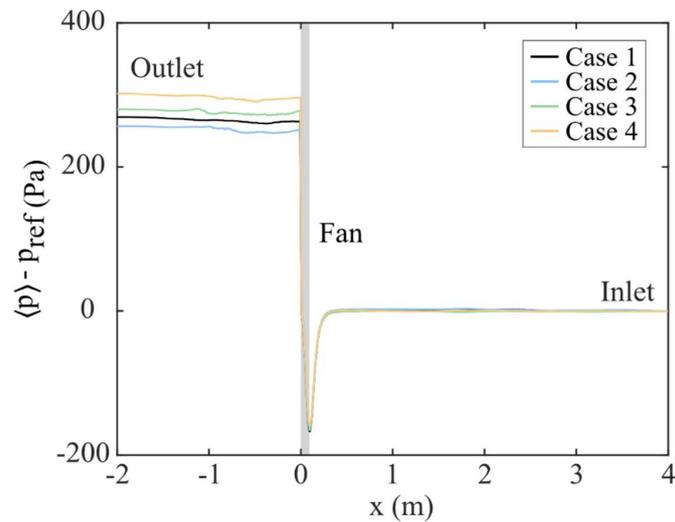
Figure 18. The pressure along the axial axis of the fan across the computational domain. x = −2 corresponds to the location near the outlet and x = 4 near the inlet. The fan location is marked out with the gray zone.

Figure 19 shows the instantaneous pressure in a plane, i.e., approximately the midspan of the blades (see Figure 14). The pressure increase in the channel between two neighboring blades is largest in Case 4. This also demonstrates the phenomenon observed in Figure 18 that the pressure at the fan outlet is highest in Case 4. Unlike Case 4, there are significant pressure fluctuations near the BTE in Cases 1-3. It is known that the fluctuating pressure distribution is caused by turbulent structures in the flow and affects the fan performance.
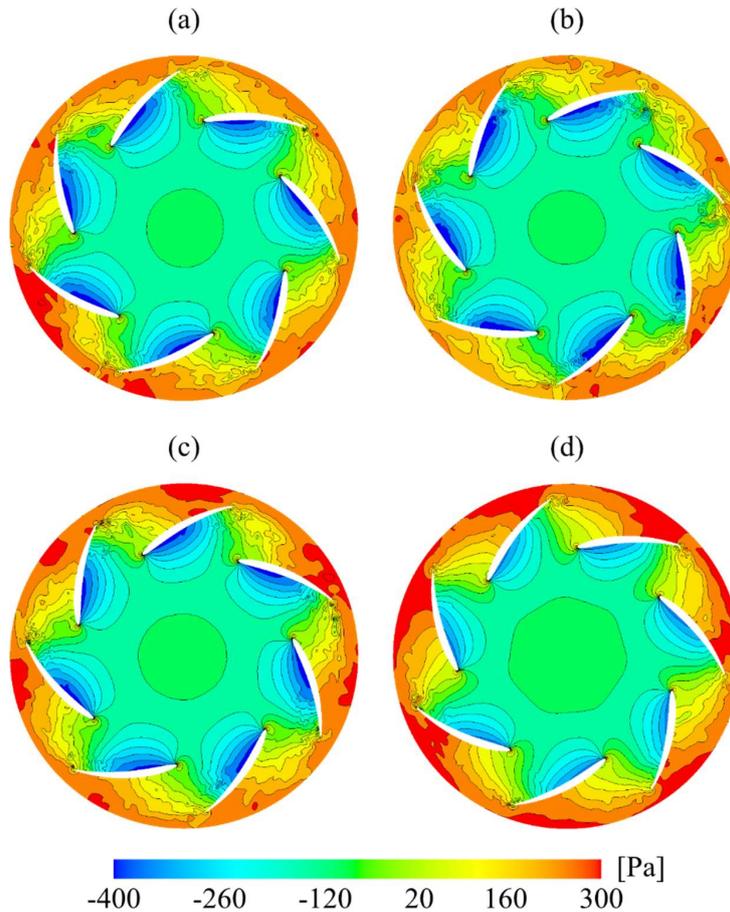
Figure 19. The instantaneous pressure in Plane 3: a) Case 1, b) Case 2, c) Case 3, and d) Case 4.

3.5 Inlet gap effect on turbulence (Paper III and Paper IV)

The RMS pressures at the monitoring line at the BLE are illustrated for all cases in Figure 20a. The line follows the blade rotation and the surface pressure is monitored during 12 fan revolutions. At the position nearest the shroud (Plane 1), the highest RMS pressure is observed for all cases. The RMS pressures have the same physical behavior for all four cases, i.e. when the distance to the shroud increases, the RMS pressure decays. From Plane 1 to the backplate, Case 2 has the lowest RMS pressure, and Case 4 the highest. At the backplate, Case 4 has the highest RMS pressure, and the other cases have almost the same.

The time-averaged surface pressures at the BLE are shown at different positions for all cases in Figure 20b. The maximum values for all cases occur at Plane 1 (shroud), whereas at the backplate the values are negative. The amplitudes of the maximum and minimum pressure (error bar) are largest at Plane 1 and they decay when the distance from the shroud increases, for all cases. At Plane 1, Case 4 has the highest amplitude. Case 2 has the lowest amplitudes at all positions. At Plane 2 and 3, the maximum positive fluctuations are larger than the

20

magnitude of the negative ones, and it is the same for all cases. It is clear that Case 2 has the smallest pressure fluctuations at the BLE.
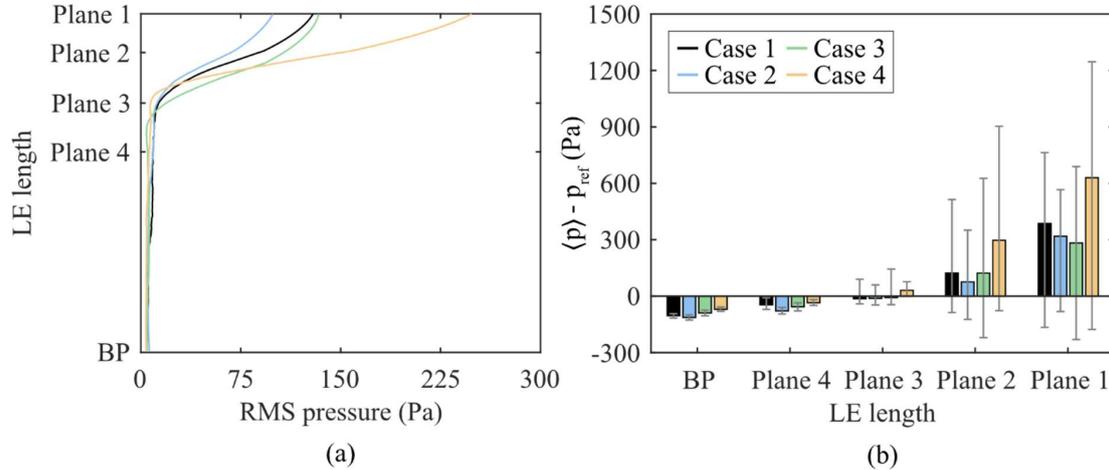

Figure 20. a) The RMS values of the pressure fluctuations for 12 fan revolutions, on one blade at the monitoring line in Figure 15a, i.e. BLE; b) the time-average pressure and error bars showing the minimum and maximum pressure. Here, BP denotes to the backplate.

In Figure 12, it was shown that using URANS and a coarse mesh the PSD of the noise at the tonal frequency, BPF, was in closer agreement upstream of the fan (M1) than downstream (M2). Using IDDES and a much finer mesh the SPL of the noise at the microphone M1 is compared in Figure 21. The highest BPF amplitude is observed for Case 4, which is 4 dB higher than Case 1. Comparing Cases 1-3 where only the gap width is changed, Case 2 with the largest gap width has the lowest BPF magnitude, and Case 1 with the medium gap width has the medium BPF magnitude. This indicates that increasing the gap width leads to a reduction in the tonal noise generation. In contrast to Cases 1-3, Case 4 produces larger tonal noise at the BPF. The reason for this might be that the longer gap wall in Case 4 triggers more stretched vortices compared with Case 1. These results agree with the results from Figure 20, where Case 2 had the lowest RMS pressure on the BLE.
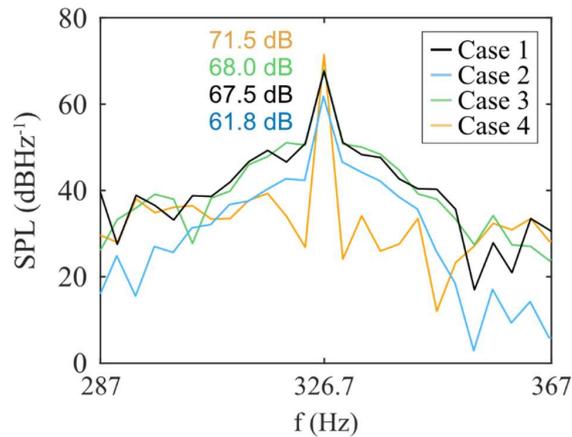
Figure 21. The SPL of the sound pressure at the microphone M1 upstream of the fan. The tonal frequency BPF = 326.7 Hz. The SPL values of the tones are presented.

Based on the band-filtered PSD of surface pressure fluctuations, the location and magnitudes of dominant tonal noise sources are evaluated. The results at the tonal frequency of BPF = 326.7 Hz are illustrated in Figure 22. The location of the highest surface pressure fluctuations is at the same position (the top of the BLE that is connected to the shroud) for all cases. Besides, this position was found to have the highest RMS pressure, see Figure 20a. The differences between the Cases are the maximum magnitude and the size of the high-magnitude region. Case 4 has the largest sound pressure (see Figure 21), and it has also the largest area and magnitude at the tonal frequency. The high energy locations are consistent with the RMS pressure fluctuations indicated in Figure 20a.

Additionally, in Cases 1, 2, and 3, small magnitudes of pressure fluctuations are seen at the BTE close to the shroud. In contrast, Case 4 does not show such a region. This agrees with the findings in Figure 19, where surface pressure fluctuations were found at the same location for Cases 1, 2, and 3 but not for Case 4.
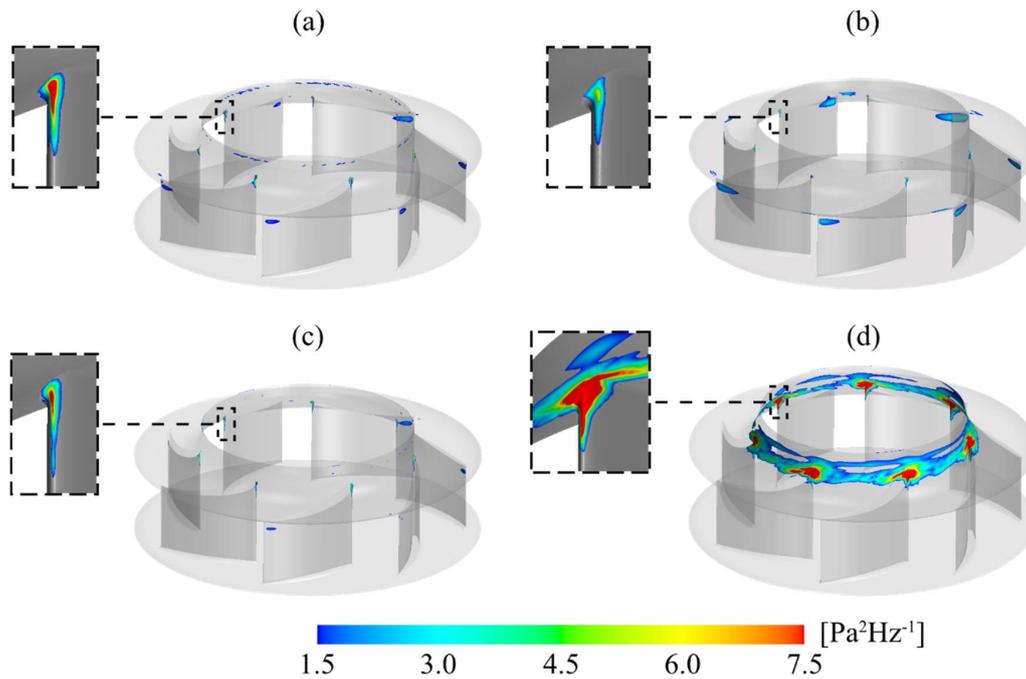
Figure 22. The PSD of surface pressure fluctuations at BPF = 326.7 Hz. a) Case 1, b) Case 2, c) Case 3, and d) Case 4.

3.6 Low-frequency rotation influences of inlet gap (Paper V)

In Figure 19, major pressure fluctuations were found near the BTE, this phenomenon is investigated for Case 1. A snapshot of isosurfaces of $p = 340\ Pa$ and contours of the velocity magnitudes at the gap are illustrated in Figure 23a. Note that in the fan passages, $340\ Pa$ is comparatively high pressure. As seen in the figure, regions of high pressure (colored orange) are found at the pressure side of Blades 2 and 3 close to the BTE. The high pressure is unevenly distributed among the fan passages. The velocity magnitudes are also unevenly distributed at the gap, where clear low and high-velocity regions are indicated.

Figure 23b shows the high-pressure regions of $p = 340\ Pa$, streamlines of the velocity magnitudes, and the velocity magnitudes at the gap. There are regions with high pressure at Blade 2. The streamlines from the gap show a flow separation and that the pressure region is formed by the flow through the low-velocity magnitude region at the gap. At the same time, there are no regions with high pressure at Blade 6. At this blade, the streamlines from the gap follow Blade 6 and shroud intersection smoothly. The turbulence initialized at the gap affects the flow at the blade and shroud intersection on the pressure side of the blades.
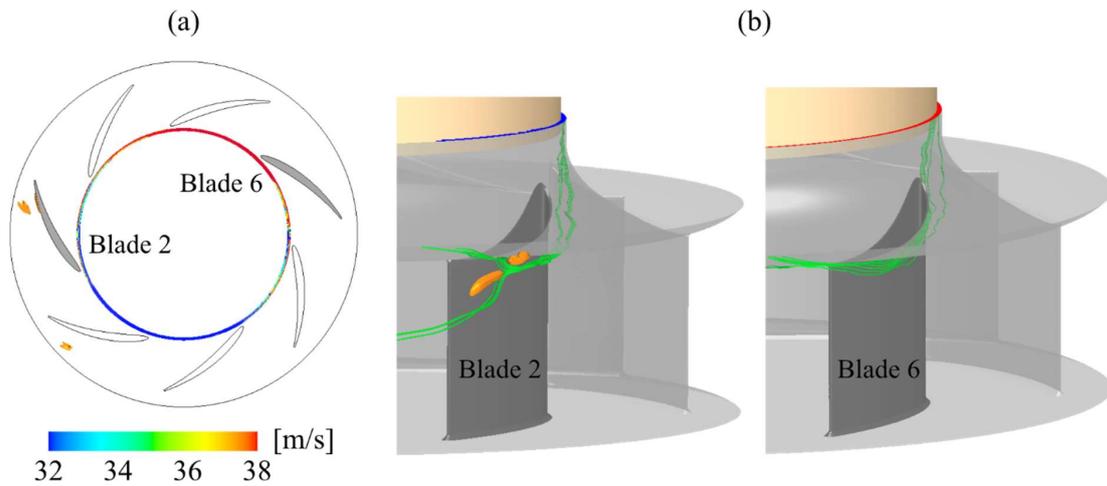
Figure 23. Iso-surface of $p = 340\ Pa$ colored orange, and contours of a) the velocity magnitudes at the gap. b) Streamlines from the gap at Blades 2 and 6, and contours of the velocity magnitudes at the gap.

A monitor point, P1, is set to observe pressure, as illustrated in Figure 24a. P1 is located on Plane 3, i.e. approximately at the midspan of the blades. The time history of the pressure at P1 is displayed in Figure 24b. P1 follows the fan rotation and the time history is shown over 25T, where T = 0.0214 s is one fan rotation period. The instantaneous pressure is fitted with a Gaussian function with a smoothing factor of 0.87 and is colored in red. A low-frequency fluctuation is found with a time period of 0.43 s. It indicates that a low-frequency rotation in relation to the fan rotation takes place in the fan and that the period time is approximately 0.43 s ≈ 20T.
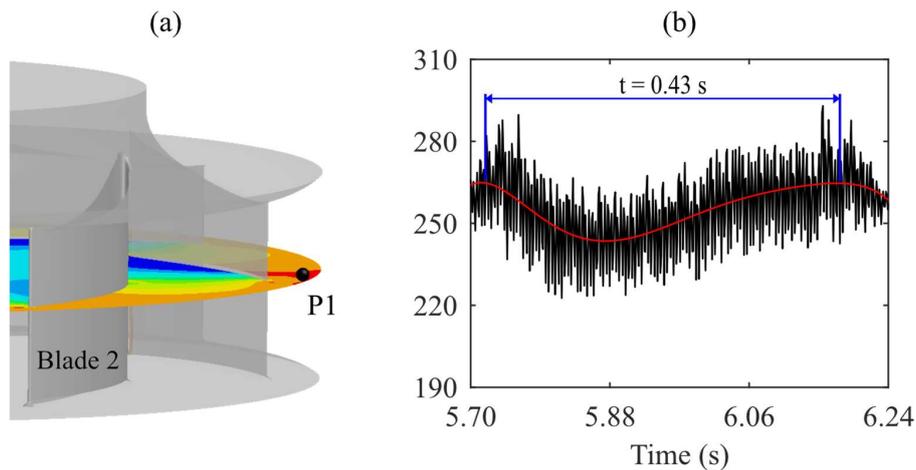

Figure 24. a) Monitor point P1. b) The time history of the pressure at P1. The red line is a Gaussian function fitted to the instantaneous pressure.

Figure 25 illustrates snapshots of the velocity magnitudes at the gap, the pressure in Plane 2, and the surface pressure on Blade 3. Here, Blade 3 is colored black to illustrate the blade position. There are regions with low-velocity magnitudes at the gap, high-pressure regions in Plane 3, and regions with high surface pressure on Blade 3, which move with the same angular speed. This region appears at the same position, at t_0 and $t_0 + 20T$, which supports the finding in Figure 24b.

The regions with high pressure always occur at the same circumferential position as the regions with low-velocity magnitudes. This phenomenon can be explained based on streamlines illustrated in Figure 23. The flow through the gap causes turbulent flow structures which are unevenly distributed among the blades. Regions with high pressure always occur at the blades where the flow separates. It is concluded that the region of high pressure is connected to flow separation caused by the low-velocity region at the gap.
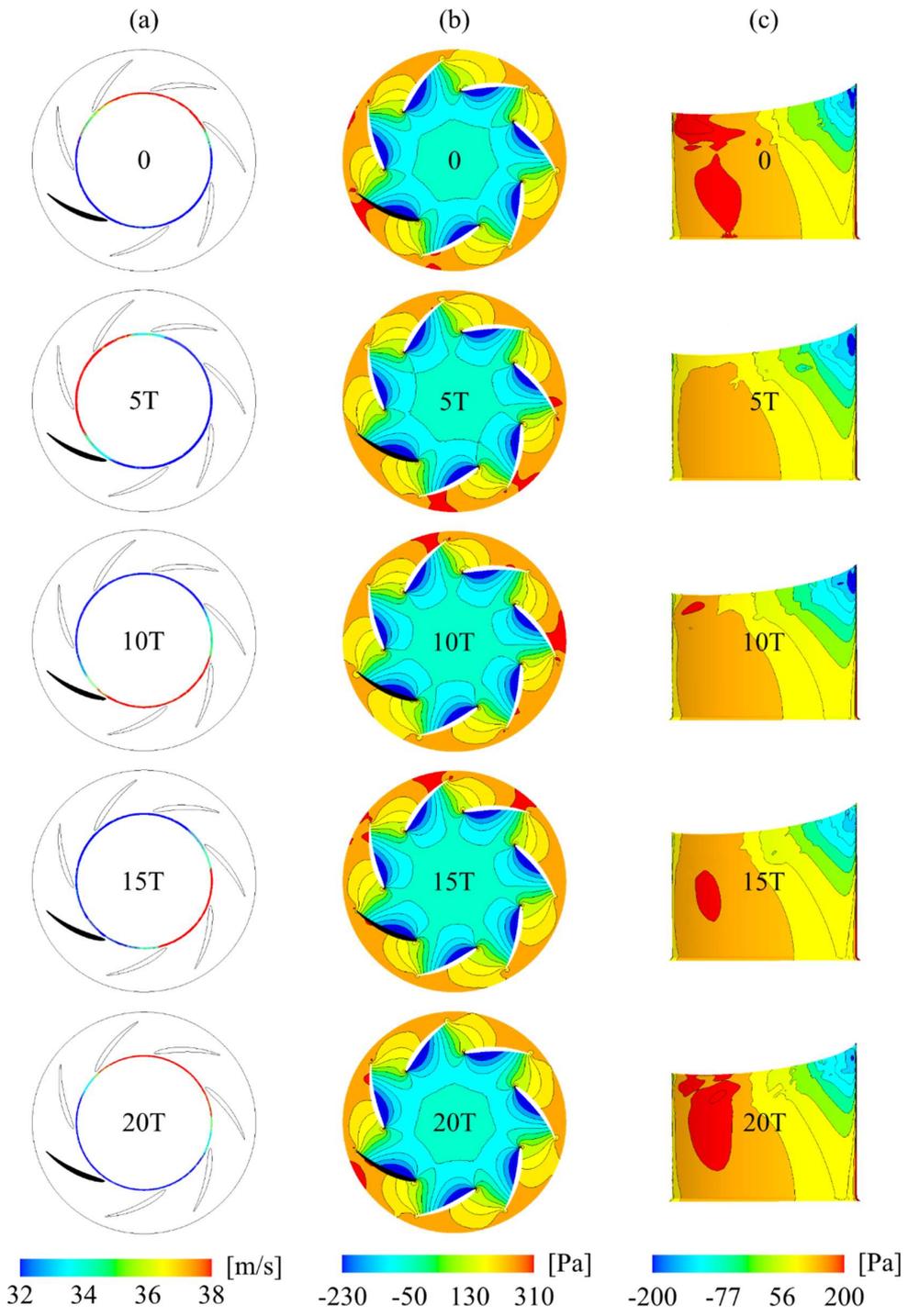
Figure 25. Snapshots of a) velocity magnitudes at the gap, b) the pressure in Plane 2, and c) the surface pressure on Blade 3. The blade colored black displays Blade 3.

26

4. Conclusion

Flow recirculation is found at the suction side of the blade close to the shroud. It is associated with the gap between the shroud and the inlet duct. The recirculating flow can influence the fan efficiency and generates tonal noise.

Different pressure distributions among the blades are found and ascribed to the turbulence originating from the inlet gap. The turbulence develops along the shroud wall and interacts with the blades at the BLE. The interaction renders uneven surface pressure distributions among the blades as well as significant peak differences. The peak values are related to the intensive levels of the resolved turbulence. As the distances to the inlet gap and the shroud increase, the difference of the pressure distributions among the blades decays. The reason is that the resolved turbulence from the inlet develops along the shroud. The influence of the turbulence on the blades is, therefore, largest near the shroud.

The wall-pressure fluctuations indicate that the locations of the tonal noise sources, 273 Hz, 326.7 Hz, and 653.4 Hz agree with the locations of the uneven surface pressure distributions and the significant pressure peaks, which are near the blade leading edges.

The gap design affects the aerodynamic performance and the acoustic emission in a clear contradiction. The pressure rise through the fan decreases from Case 4, Case 3, Case 1 to Case 2. However, the noise is reduced in the reverse order: Case 2, Case 1, Case 3 and Case 4. For Case 4 exhibiting the largest pressure rise, vortices are less intensive near the BTE well inside the blade passage, and at the same position, there are less pressure fluctuations. Thus, the aerodynamic performance is related to the turbulence inside the blade passage. However, Case 4 is the worst acoustic case. This is attributed to the strongest gap turbulence near the wall at the BLE. The turbulence from the gap is ingested into the blade passage and results in the strongest pressure fluctuations. The synthesis of these effects suggests the physical mechanisms that given the turbulence at the entry becomes stronger, the flow inside the blade passage is stabilized. Consequently, the fluctuations near the BTE are mitigated, resulting in improved aerodynamic performance.

Unevenly distributed regions with high pressure are found at the pressure side of the blades close to the shroud. The velocity magnitudes at the gap are also unevenly distributed, where clear low and high-velocity regions are indicated. A correlation between the high-pressure and the low-velocity magnitudes is observed, that is, the high-pressure regions occur downstream of the region of the low-velocity magnitude. Intensive turbulent flow structures are developed from the low-velocity region and are swept along the intersection between the blade and

shroud, on the pressure side of the blade. Eventually, the turbulence gives rise to flow separation with a high-pressure region near the BTE. This unsteady flow behavior revolves around the fan rotation axis. And its period is 5% of the fan rotation speed, based on the analysis of the time history of the gap velocity magnitudes and the evolution of the high-pressure region. The same frequency of the high pressure was also found in previous experimental measurements

5. Reference

[1] T. Roberts, "We Spend 90% of Our Time Indoors. Says Who?," Retrieved from https://www.buildinggreen.com/blog/we-spend-90-our-time-indoors-says-who, (2016).

[2] B. Berglund, T. Lindvall, and D. Schwela, "New Guidelines for Community Noise," Noise & Vibration Worldwide **31**, 24-29 (2000).

[3] M. Azimi, "Noise Reduction in Buildings Using Sound Absorbing Materials," Journal of Architectural Engineering Technology **6,** (2017).

[4] J. Seabi, K. Cockcroft, P. Goldschagg, and M. Greyling, "A prospective follow-up study of the effects of chronic aircraft noise exposure on learners' reading and comprehension in South Africa" Journal of Exposure Science and Environmental Epidemiology **25**, (2015).

[5] M. Klatte, K. Bergstrom, and T. Lachmann, "Does noise affect learning? A short review on noise effects on cognitive performance in children" Frontiers in Psychology **4**, (2013).

[6] L.M. Wang and C.C. Novak, "Human performance and perception-based evaluations of indoor noise criteria for rating mechanical system noise with time-varying fluctuations," ASHRAE Transaction **116,** 553-568 (2010).

[7] M. Tautz, "Aeroacoustic Noise Prediction of Automotive HVAC System," FAU Forschungen, Reihre B, Medizin, Naturwissenschaft, Technik Band 27. Erlangen: FAU University Press (2019).

[8] W. P. Jones, "Air conditioning applications and design," 2 ed. Arnold 294-295 (1997).

[9] J.E. Ffowcs Williams and D.L. Hawkings, "Theory relating to the noise of rotating machinery," Journal of Sound and Vibration **10,** 10-21 (1969).

[10] D. Wolfram and T.H. Carolus, "Experimental and numerical investigation of the unsteady flow field and tone generation in an isolated centrifugal fan impeller," Journal of Sound and Vibrations **329,** 4380-4397 (2010).

[11] V. Pommier-Budinger and O. Cherrier, "Baffle silencer with tunable resonators for adaptive control of variable tonal noise," Journal of Vibration and Control **21,** 1801-1809 (2015).

[12] Lighthill M.J. On Sound Generated Aerodynamically. I General Theory. Proc. R. Soc. Lond. A 1952;211:564-587.

[13] Ansys Inc. Fluent User Guide (Version 19.0) 2018.

[14] M.L. Shur, P.R. Spalart, M.K. Strelets, and A.K. Travin, "A hybrid RANS-LES approach with delayed-DES and wall-modelled LES capabilities," Int. J. Heat Fluids Flow 29, 1638-1649 (2008).

[15] P. Spalart, S. Deck, M. Shur, K. Squires, M. Strelets, and A. Travin, "A new version of detached-eddy simulation, resistant to ambiguous grid densities," Theoret. Comput. Fluid Dynamics 20, 181-195 (2006).

[16] J.H. Ferziger and M. Peric, "Computational Methods for Fluid Dynamics," 3rd rev. ed., Springer-Verlag, Berlin (2002).

[17] Siemens PLM Software. STAR-CCM+ User Guide (Version 12.04) 2017.

[18] H.-D. Yao andL. Davidsson, "Vibro-acoustics response of simplified glass window excited by the turbulent wake of a quarter-spherocylinder body," The Journal of the Acoustical Society of America 146, 3163-3176 (2019).

[19] A. Rynell, G. Efraimsson, M. Chevalier, and M. Åbom, "Inclusion of upstream turbulent inflow statistics to numerically acquire proper fan noise characteristics," SAE Technical Paper 2016-01-1811 (2016).

[20] A. Rynell, M. Chevalier, M. Åbom, and G. Efraimsson, "A numerical study of noise characteristics originating from a shrouded subsonic automotive fan," Applied Acoustics 140, 110-121 (2018).

[21] K.S. Brentner and F. Farassat, "Analytical comparison of the acoustic analogy and Kirchhoff formulation for moving surfaces," AIAAA J 36, 1379-86 (1998).

[22] W. Neise, "Review of fan noise generation mechanisms and control methods," In: Proceedings of the Fan Noise 1992 International Symposium, Senlis, France. 45-56 (1992).

[23] M. Younsi, F. Bakir, S. Kouidri, and R. Rey "Numerical and experimental study of unsteady flow in a centrifugal fan," In proceedings of the 7th European Turbomachinery Conference, Athens, Greece, 2007, 175-189 (2007).

[24] S. Salunkhe, O.E Fajri, S. Bhushane, D. Thompson, D. O´Dohety, T. O´Dohety, and A. Mason-Jones, "Validation of tidal stream turbine wake predictions and analysis of wake recovery mechanism," Journal of Marine Science and Engineering 7, (2019).

[25] M. Sanjose and S. Moreau, "Direct noise prediction and control of an installed large low-speed radial fan," European Journal of Mechanics 61, 235-243 (2017).

[26] A. Lawrenson, G. Berg, C. Carlsson, M. Fransson, L. All, inventors; Swegon AB, applicant, "Low profiled AHU with tilted rotary heat exchange," International patent WO 2010085197, (2010)

[27] Y. Lee, "Impact of fan gap flow on the centrifugal impeller aerodynamics," Journal of Fluids Engineering 132, 1-9 (2010).